



Crustal Deformation and Fault Models of the 2016 Kumamoto Earthquake Sequence: Foreshocks and Main Shock

Tomokazu Kobayashi, Hiroshi Yarai, Satoshi Kawamoto, Yu Morishita, Satoshi Fujiwara, and Yohei Hiyama

Abstract

We explored crustal deformation associated with the foreshocks and the main shock of the 2016 Kumamoto earthquake sequence. We conducted kinematic-Global Navigation Satellite System analysis for the foreshocks, and succeeded in separately retrieving the coseismic crustal deformation for the two M₆-class events that occurred nearly contemporaneously (within 3 h). Our fault model shows that the first seismic event occurred in the northern part of the Takano-Shirahata segment of the Hinagu Fault, while the second occurred in the southern part of the segment. For the main shock, we mapped the widely distributed ground displacements in and around the Futagawa Fault zone by conducting an Interferometric Synthetic Aperture Radar analysis. The obtained displacement field shows clear displacement boundaries linearly along the Futagawa and the Hinagu faults, across which the sign of the displacement component turns to the opposite, suggesting that the two faults were intimately involved with the main shock. The previously known fault trace of the Futagawa Fault terminates at the western edge of the Aso Caldera, but the intense deformation implying fault ruptures clearly appears within the caldera. Our fault model suggests that the main rupture occurred on the Futagawa Fault in a right-lateral fashion with normal faulting. The rupture on the Futagawa Fault extends into the Aso Caldera, and the fault plane dips oppositely toward the southeast, suggesting that the rupture propagates eastward on a conjugate fault against the main fault. The rupture on the Hinagu Fault shows a right-lateral fault motion on a plane dipping west.

Keywords

Crustal deformation · Fault model · InSAR · Kinematic-GNSS · Kumamoto earthquake

1 Introduction

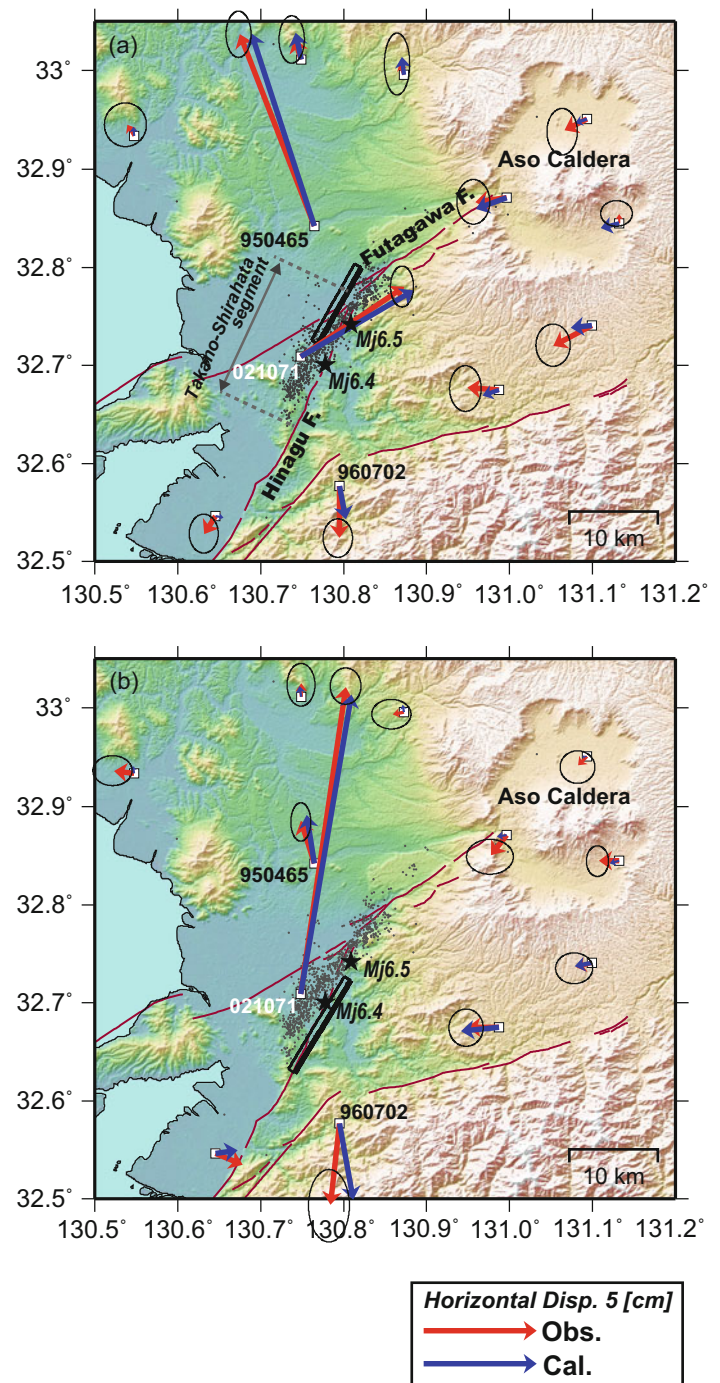
The 2016 Kumamoto earthquake sequence started with an event of a Japan Meteorological Agency (JMA) magnitude (M_j) of 6.5 at 12:25 (Coordinated Universal Time: UTC) on

T. Kobayashi (✉) · H. Yarai · S. Kawamoto · Y. Morishita · S. Fujiwara
Geospatial Information Authority of Japan, Tsukuba, Ibaraki, Japan
e-mail: kobayashi-t96dv@mliit.go.jp

Y. Hiyama
Ministry of Land, Infrastructure, Transport and Tourism, Chiyoda-ku, Tokyo, Japan

April 14, 2016, followed by an M_j 6.4 event ~2.5 h later at 14:06 (UTC). After the M₆-class foreshocks, the main shock of M_j 7.3 occurred at 16:25 (UTC) on April 15, 2016. The foreshocks ruptured the Takano-Shirahata segment of the Hinagu Fault, which connects with the Futagawa Fault, while the main shock ruptured mainly the Futagawa Fault as well as other faults in a complex manner (Fig. 1). The detailed source properties provide fundamental information for better understanding of the 2016 Kumamoto earthquake sequence. However, a few points remain unclear: (1) The two M₆ foreshocks occurred within a few hours of each other; hence, conventional geodetic data cannot retrieve the individual coseismic deformation separately because of the

Fig. 1 Coseismic displacements due to (a) the $M_j6.5$ event and (b) the $M_j6.4$ event estimated from kinematic-GNSS positioning data, respectively. Arrows represent horizontal displacement. Red and blue represent the observed and the model-predicted displacement, respectively. Error ellipses show the standard deviation (1σ) for the observed displacements. Stars indicate epicenters of the $M_j6.5$ and $M_j6.4$ events. The frames indicate surface projections of the fault plane for modeling and the thick line represents the upper edges. Red lines indicating active faults are from the Headquarters for Earthquake Research Promotion (2013)



limited temporal resolution, which prevents construction of each fault model. (2) A number of fault models for the main shock have been proposed from seismological and/or geodetic analyses, but there are few that elaborately consider fault ruptures in the Aso Caldera. Crustal deformation data with high temporal and spatial resolution will be useful to clarify the unclear source properties of the foreshocks and the main shock, respectively.

This study consists of (1) fault modeling of the $M_j6.5$ and $M_j6.4$ foreshocks and (2) fault modeling of the main shock. For the analyses, we used kinematic-GNSS data to separately retrieve the coseismic displacement of the two individual foreshocks, and for the main shock we used Interferometric Synthetic Aperture Radar (InSAR) data to map the complicated ground displacement field.

2 Foreshocks: $M_j6.5$ and $M_j6.4$

2.1 Crustal Deformation Derived by Kinematic-GNSS

The Geospatial Information Authority of Japan (GSI) releases some types of Global Navigation Satellite System (GNSS) positioning data. Q3 data, which is the fastest-derived static positioning data, are calculated every 3 h with a 6-h data window (Nakagawa et al. 2009). However, the time interval between the $M_j6.5$ and $M_j6.4$ events is less than 3 h; hence, we cannot separate the coseismic displacement caused by the two events that occurred in temporal proximity. Thus, to overcome the issue of the temporal resolution, we used kinematic-GNSS data to retrieve the coseismic crustal deformation of the two individual foreshocks separately. We obtained post-processed kinematic positioning results using the International GNSS Service (IGS) final orbit and an elevation cutoff angle of 15° . The data are the same coseismic data presented in Kawamoto et al. (2016).

Figure 1a, b show coseismic horizontal displacement vectors for the $M_j6.5$ and the $M_j6.4$ events, respectively. Red is GNSS-observed displacement. The hypocenters are close to each other, but there is a clear difference in the spatial pattern of the crustal deformation. The displacement recorded at the GNSS site 021071 reaches 5.5 cm during the $M_j6.5$ event, while it increases to ~ 13.5 cm during the $M_j6.4$ event. The orientation of the ground movement changes from NE-SW to NNE-SSW. We also recognize a difference at 950465 where the displacement reaches 9.0 cm for the $M_j6.5$ event, while for the $M_j6.4$ event it decreases to 1.9 cm. These differences strongly suggest that the main slip areas and/or slip mechanisms are different.

2.2 Fault Models

We next constructed a fault model assuming a single rectangular fault plane with a uniform slip (Okada 1985). We estimated the model parameters using a simulated annealing method (Metropolis et al. 1953; Cervelli et al. 2001). To estimate the individual confidence of the inferred parameters, we employed a bootstrap method (Efron

1979). For the analysis, the strike was assumed to run along the Hinagu Fault (search range: $200\text{--}220^\circ$ in strike angle), but both the east- and west-dipping planes were searched.

The frames in Fig. 1a, b show the estimated fault positions for the $M_j6.5$ and the $M_j6.4$ events, respectively. Blue vectors represent the model-predicted displacements. The fault model can account for the observation data well. The estimated fault parameters are listed in Table 1. For the $M_j6.5$ event, the depth (fault center) is estimated to be approximately 2.5 km at fault top, while for the $M_j6.4$ event, the depth is estimated to be 0.2 km at fault top. The $M_j6.4$ event occurred shallower than $M_j6.5$ event. Also, there is a significant difference in the horizontal position. As seen in Fig. 1, the $M_j6.5$ event occurred in the northern part of the Takano-Shirahata segment of the Hinagu Fault, which is near the junction of the Futagawa Fault and the Hinagu Fault, while the $M_j6.4$ event is estimated to have occurred south of the $M_j6.5$ event.

Matsuda (1975) proposed an empirical relation between a magnitude M and a fault length L ; $\text{Log } L = 0.6 M - 2.9$. According to the formulation, the foreshocks for the Kumamoto earthquake should have fault lengths less than 10 km. On the other hand, the fault lengths estimated in the modeling are ~ 10 km for both the events. The inconsistency may suggest that the relation does not always meet nature of fault rupture, which could be a controversial issue in future work because the formulation has been often used in discussion regarding potential of inland earthquake.

Kobayashi (2017) showed the distributed slip model for the foreshocks using InSAR and GNSS (static solution) data, in which a deep north slip and a shallow south slip with almost pure right-lateral fault motion are estimated. The author suggested a possibility that the north and south slips correspond to the $M_j6.5$ and the $M_j6.4$ events, respectively, taking the spatial relation of the hypocenters into consideration. However, InSAR data includes contributions from both events, and cannot further separate the individual crustal deformation because of its temporal resolution. We here stress that the kinematic-GNSS data work well to derive the individual source properties for the two events that occurred within a few hours of each other. The kinematic-GNSS data will have an active part in fault modeling in the future.

Table 1 Fault parameters for $M_j6.5$ (upper) and $M_j6.4$ (lower) events inferred from kinematic-GNSS data

Event	Longitude	Latitude	Depth	Length	Width	Strike	Dip	Rake	Slip	M_w
12:25 Apr. 14	130.821 (0.011)	32.800 (0.013)	2.5 (0.8)	9.9 (2.5)	2.9 (1.6)	209.5 (4.6)	72.7 (10.2)	166.5 (21.3)	1.6 (0.3)	6.03
14:06 Apr. 14	130.809 (0.013)	32.723 (0.019)	0.2 (0.9)	12.2 (3.0)	3.6 (2.3)	211.3 (5.6)	76.0 (10.1)	157.9 (15.8)	0.9 (0.4)	5.98

The units of length, width, and depth are in kilometers; those of dip, strike, and rake are in degrees; and the unit of slip is meters. The position indicates the top-left corner of the fault plane. The parenthetical numbers are the standard deviation (1σ)

3 Main Shock

3.1 InSAR- and GNSS-Derived Complex Crustal Deformation

The Japan Aerospace Exploration Agency (JAXA) conducted emergency observations from the Advanced Land Observing Satellite 2 (ALOS-2) in response to the Kumamoto earthquake. We applied an InSAR method to the ALOS-2 data acquired on April 15, 2016 and on April 29, 2016 for which we can obtain InSAR images with two different view angles from ascending/left-looking and descending/left-looking orbit data. The master images were acquired before the main shock and after the two foreshocks; thus, the InSAR images do not include the crustal deformation due to the foreshocks. In addition to InSAR, we utilized GNSS data to identify the coseismic displacement. To obtain the coseismic displacement, we calculated a difference in the daily coordinate data corresponding to observation dates of the master and slave images. To achieve stable coordinate data for the master, we averaged Q3 data from 18:00 on April 14 to 14:59 on April 15 (UTC). On the other hand, for the slave, we took an average of F3 data, which are the finest solutions (Nakagawa et al. 2009), from April 25, 2016 to May 3, 2016 (10 days).

Figure 2a, b show the InSAR images for the ascending and descending orbit data, respectively. We can identify widely distributed crustal deformation in and around the Futagawa Fault zone. Intense fringes appear on the northern side of the Futagawa Fault. They are line-of-sight (LOS) lengthening phase changes for both orbit data, suggesting that the ground subsides significantly in this area. We can identify clear displacement discontinuities along the previously known fault traces of the Futagawa Fault. In addition to the Futagawa Fault, the discontinuity can be also identified on the Hinagu fault trace, suggesting that the Hinagu Fault is also involved in the fault rupture of the main shock. It is also noted that large displacements can be recognized within the Aso Caldera. The eastern edge of the previously known Futagawa Fault terminates at the western rim of the caldera; however, InSAR images obviously show that the fault rupture proceeds into the caldera.

Figure 3a, b show the GNSS-derived deformation data. Red vectors and bars represent observed horizontal and vertical displacements, respectively. The horizontal displacement pattern surrounding the Futagawa Fault is consistent with a right-lateral slip motion. However, at site 021071 northeastward movement was detected where southward movement should be observed if right-lateral slip occurred on the Futagawa Fault, suggesting that non-negligible fault slip also occurred on the Hinagu Fault. The spatial pattern in the Aso Caldera is complicated. Although the horizontal

component shows uniform westward movement, for the vertical component, ground subsidence is dominant in the central part of the caldera, while ground uplift is observed at its western edge.

3.2 Fault Model

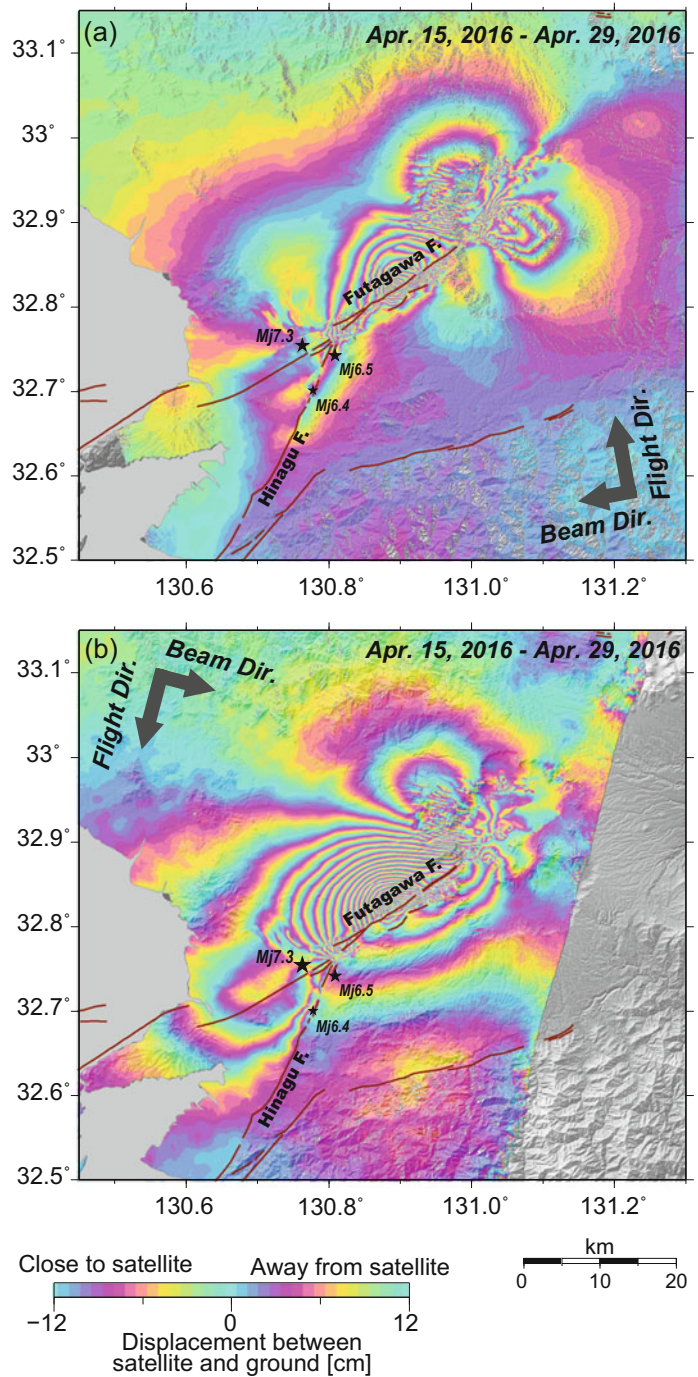
We next constructed a fault model for the main shock to obtain the source properties. We utilized derived InSAR data of both ascending and descending orbits as well as GNSS data. The interferograms have ground surface changes over a range of several tens of kilometers, producing too many values to be easily assimilated in a modeling scheme. In order to reduce the amount of data for the modelling analysis, we resampled the InSAR data beforehand, using a quadtree decomposition method. Essentially, we followed an algorithm of Jónsson et al. (2002). For a given quadrant, if, after removing the mean, the residual is greater than a prescribed threshold, the quadrant is further divided into four new quadrants. The threshold was set to 2 cm. This process is iterated until either each block meets the specified criterion, or until the quadrant reaches a minimum block size of 16×16 pixels, equivalent to $\sim 30 \times \sim 30$ m.

For the weight of modeling, we assigned standard deviations of 1.5 and 1.1 cm for the ascending and descending InSAR data, respectively, calculated using phase changes outside of the source region. For GNSS data, we provided the standard deviations of the time series data during the averaged period; 0.4, 0.5, and 0.9 cm for the EW, NS, and UD components, respectively. We estimated the model parameters using a simulated annealing method in nearly the same manner as the analysis for the foreshocks.

Here we set the fault planes for the Futagawa and Hinagu faults, whose strike angles are fixed to be 235° and 205° so as to fit the displacement discontinuities, respectively. In addition to the two faults, we set one more fault which is in the eastward extension of the Futagawa Fault within the Aso Caldera. For the modeling, both the NW- and SE-dipping fault planes are searched (strike angle: from 225° to 245° /from 45° to 65°), and neither the dip nor the rake were constrained. The fault planes for the Futagawa Fault, its eastward extension fault, and the Hinagu Fault are hereafter termed F1, F2, and F3.

Figure 4 shows the InSAR results calculated from the derived fault model. The model can account for the broad spatial pattern although there still remain residuals in the proximity of the faults (Fig. 2). The GNSS data are also reproduced well by the constructed model (Fig. 3). The estimated parameters are listed in Table 2. The total seismic moment is 4.76×10^{19} Nm (M_w 7.05) assuming a rigidity of 30 GPa, and the released moments for each fault are

Fig. 2 Interferograms for (a) ascending/left-looking and (b) descending/left-looking orbit data, respectively. Stars indicate the epicenters of the main shock and the two foreshocks



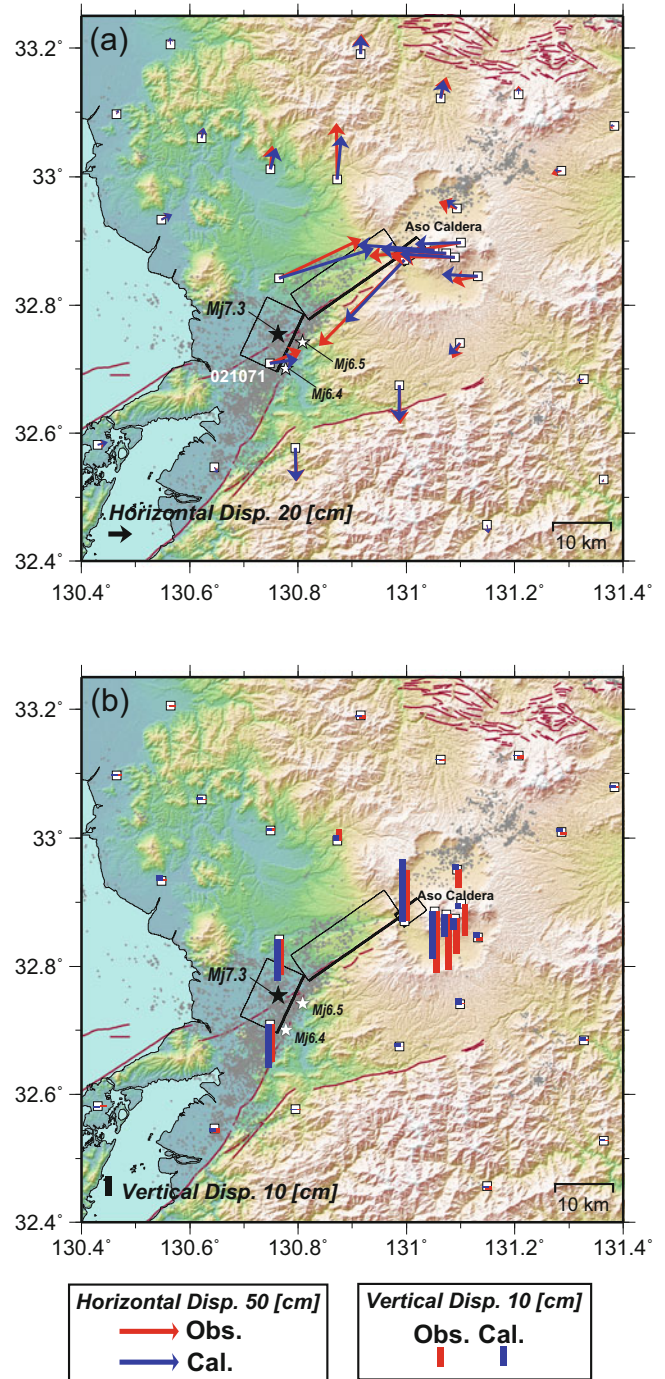
estimated to be 2.84×10^{19} Nm (M_w 6.90), 3.37×10^{18} N m (M_w 6.28), and 1.58×10^{19} N m (M_w 6.73) for F1, F2, and F3, respectively. According to the results of the JMA CMT solution, the seismic moment is 4.06×10^{19} N m (M_w 7.0) (JMA 2016). Our result is in good agreement with this value.

For the F1 fault, right-lateral slip is predominant, but a normal fault motion is also included. The normal slip

possibly produces the ground subsidence on the northern side of the Futagawa Fault. The dip angle is neither high nor low, but is moderate. Approximately 56% of the total seismic moment is released on this fault.

The F2 fault also has a right-lateral slip component. Of note, the fault was determined to be not NW-dipping but SE-dipping planes (Fig. 4). Unfortunately, the aftershock is in low level activity around the F2 as seen in Fig. 3, thus we

Fig. 3 Coseismic displacements of the main shock in (a) horizontal and (b) vertical components, respectively. Arrows and bars represent horizontal and vertical displacements, respectively. Red and blue represent the observed and the model-predicted displacement, respectively. Stars indicate epicenters of the main shock and the two foreshocks. Gray dots represent the epicenters of aftershocks



cannot confirm the fault dip from the hypocenter distribution. Hence, to confirm the reliability of the SE-dipping plane, we investigate root mean squares (RMSs) of residuals for various dip angles of F2. For the estimate, we assigned dip angles with an interval of 20° , and searched for the optimal parameters in the same manner. We here fixed the parameters of F1 and F3. For the NW-dipping model, the RMSs are estimated to be 15.7, 15.8, 17.0, and 16.4 cm for the dip angle of 20° , 40° , 60° , and 80° respectively. On the other hand, for the SE-dipping model, the RMSs are

15.6, 15.2, 15.1, and 15.5 cm for the dip angle of 20° , 40° , 60° , and 80° , respectively. We can find that the residuals systematically decrease with approaching to the moderate dip angle for the SE-dipping plane. The results suggest that the fault plane drastically changes to the opposite dip at the western margin of the Aso Caldera. The fault rupture probably proceeds on a conjugate fault against the main fault.

The F3 fault has a nearly pure right-lateral motion. If there were no slip on the Hinagu Fault, the GNSS site

Fig. 4 Same as Fig. 2 but for the LOS displacements calculated by the fault model. The frames indicate surface projections of the fault plane for modeling and the thick line represents the upper edges

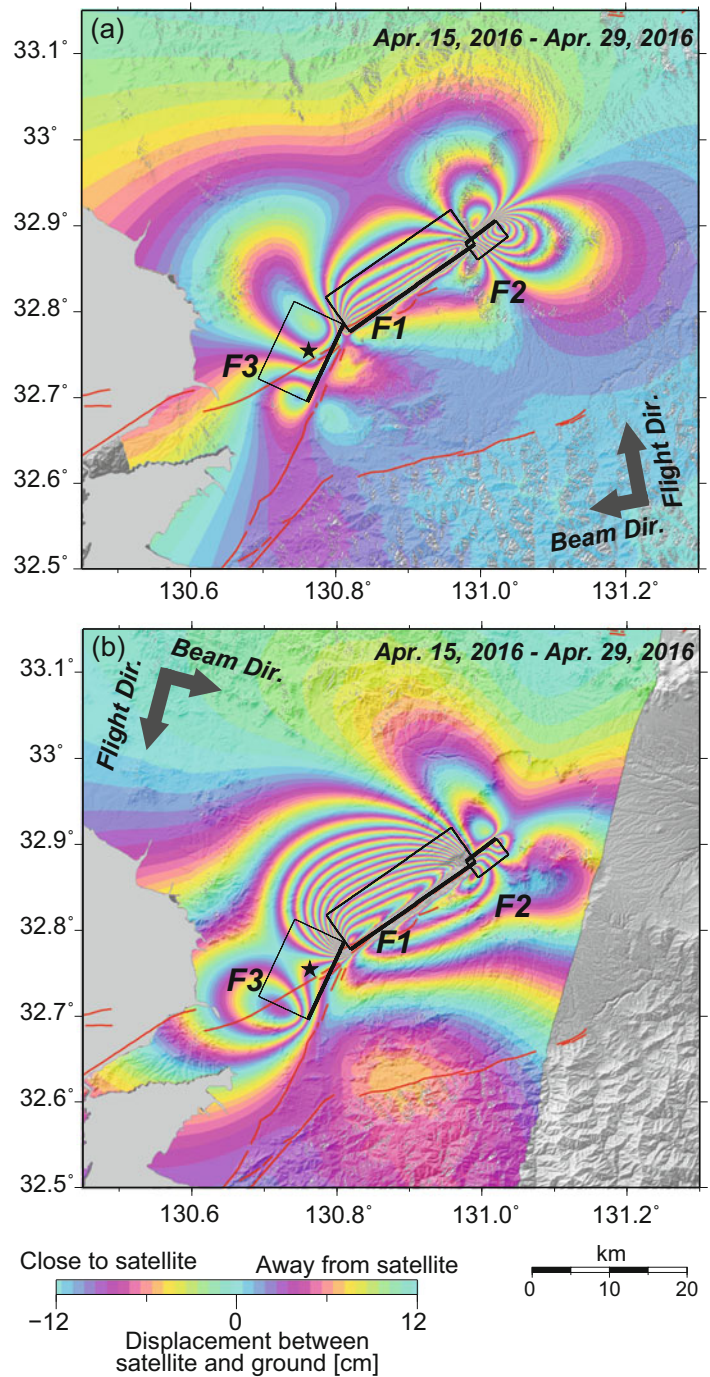


Table 2 Fault parameters for the main shock

Fault	Longitude	Latitude	Depth	Length	Width	Strike	Dip	Rake	Slip	M_w
F1	130.992 (0.011)	32.879 (0.002)	6.0 (0.2)	19.7 (0.8)	12.3 (0.5)	235	63.9 (4.2)	-151.0 (2.0)	3.9 (0.2)	6.90
F2	130.979 (0.013)	32.880 (0.009)	4.9 (0.9)	4.9 (1.6)	6.4 (4.8)	52.7 (4.0)	65.9 (18.2)	-169.9 (6.6)	3.6 (0.8)	6.28
F3	130.811 (0.010)	32.786 (0.010)	11.3 (0.8)	11.0 (1.0)	19.9 (5.3)	205	69.4 (8.8)	178.0 (7.5)	2.4 (0.1)	6.73

The units of length, width, and depth are in kilometers; those of dip, strike, and rake are in degrees; and the unit of slip is meters. The position indicates the top-left corner of the fault plane. The parenthetical numbers are the standard deviation (1σ)

021071 would move southward. This is why the slip of the Hinagu Fault is essential to account for the observed eastward motion.

Acknowledgements ALOS-2 data were provided by the Earthquake Working Group under a cooperative research contract with the Japan Aerospace Exploration Agency (JAXA). ALOS-2 data are owned by JAXA. Generic Mapping Tools (GMT) provided by Wessel and Smith (1998) were used to construct the figures. Hypocenter data processed by the Japan Meteorological Agency (JMA) were used. Part of the GNSS data was provided by the JMA. We thank the editor and two anonymous reviewers for their constructive comments.

References

- Cervelli P, Murray MH, Segall P, Aoki Y, Kato T (2001) Estimating source parameters from deformation data, with an application to the March 1997 earthquake swarm off the Izu Peninsula, Japan. *J Geophys Res* 106:11217–11237
- Efron B (1979) Bootstrap methods: another look at the jackknife. *Ann Statist* 7:1–26
- Headquarters for Earthquake Research Promotion (2013) Evaluation of active faults to date. http://jishin.go.jp/main/chousa/katsudansou_pdf/93_futagawa_hinagu_2.pdf. Accessed 8 Oct 2017 (in Japanese)
- Japan Meteorological Agency (2016) CMT catalog. <http://www.data.jma.go.jp/svd/eqev/data/mech/cmt/fig/cmt20160416012505.html>. Accessed 10 Oct 2017. (in Japanese)
- Jónsson S, Zebker H, Segall P, Amelung F (2002) Fault slip distribution of the 1999 Mw 7.1 Hector mine, California, earthquake, estimated from satellite radar and GNSS measurements. *Bull Seismol Soc Am* 92:1377–1389
- Kawamoto S, Hiyama Y, Ohta Y, Nishimura T (2016) First result from the GEONET real-time analysis system (REGARD): the case of the 2016 Kumamoto earthquakes. *Earth Planets Space* 68:190. <https://doi.org/10.1186/s40623-016-0564-4>
- Kobayashi T (2017) Earthquake rupture properties of the 2016 Kumamoto earthquake foreshocks (Mj6.5 and Mj6.4) revealed by conventional and multiple-aperture InSAR. *Earth Planets Space* 69:7. <https://doi.org/10.1186/s40623-016-0594-y>
- Matsuda T (1975) Magnitude and recurrence interval of earthquakes from a fault. *J Seismol Soc Jpn*, 2 28:269–283 (in Japanese with English abstract)
- Metropolis N, Rosenbluth A, Rosenbluth M, Teller A, Teller E (1953) Equation of state calculations by fast computing machines. *J Chem Phys* 21:1087–1092
- Nakagawa H, Toyofuku T, Kotani K, Miyahara B, Iwashita C, Kawamoto S, Hatanaka Y, Munekane H, Ishimoto M, Yutsudo T, Ishikura N, Sugawara Y (2009) Development and validation of GEONET new analysis strategy (Version 4). *J Geogr Surv Inst* 118:1–8 (in Japanese)
- Okada Y (1985) Surface deformation due to shear and tensile faults in a halfspace. *Bull Seismol Soc Am* 75:1135–1154
- Wessel P, Smith WH (1998) New, improved version of generic mapping tools released. *Eos Trans AGU* 79:579